# Charge-state evolution from $W^{5+}$ to $W^{7+}$ at energies below the ionization potentials

C. L. Yan ⬡, Q. Lu, Y. M. Xie, B. L. Li, N. Fu ⬡, Y. Zou, C. Chen, and J. Xiao ⬡[*]

*Shanghai EBIT Laboratory, Key Laboratory of Nuclear Physics and Ion-Beam Application (MOE), Institute of Modern Physics,*
*Fudan University, Shanghai 200433, China*

Experiments on an electron-beam ion trap (EBIT) and calculations using flexible atomic code (FAC) are carried out to study the charge-state evolution from $W^{5+}$ to $W^{7+}$. The $W^{7+}$ line at 574.47 nm is observed with an electron-beam energy of about 48 eV, which is far below the ionization potentials of $W^{5+}$ (65 eV) and $W^{6+}$ (122 eV). Multicharge-state collisional-radiative (CR) calculations for $W^{5+}$, $W^{6+}$, and $W^{7+}$ are performed with level-to-level processes with configuration interaction (CI), including direct ionization, collision excitation, radiative recombination, charge exchange, radiative transition, and autoionization. The CI strongly influences the calculated ionization cross sections for metastable levels. The CR-simulated spectra agree well with the experiments, and the calculated effective ionization cross section for $W^{6+}$ has the same trend as the available experimental data [M. Stenke *et al.*, J. Phys. B: At. Mol. Opt. Phys. **28**, 2711 (1995)]. The metastable levels (~40 eV for $W^{5+}$; ~40 and ~85 eV for $W^{6+}$) significantly contribute to the ionization through excitation-autoionization at rather low energies (<50 eV) in the EBIT plasma. These metastable levels could have a considerable influence on the charge-state evolution of tungsten ions in edge fusion plasma.

## I. INTRODUCTION

Tungsten is considered as a suitable plasma-facing material for fusion devices [1], where tungsten impurities are sputtered and ionized to different charge states depending on the plasma temperature ranging from several eV at the edge to 30 keV in the core [2–4]. Emission from the tungsten ions causes undesirable radiative power losses. Moreover, the diagnostics and control of the edge plasma are required for the steady-state operation of a fusion plasma [5]. Hence, much effort has been expended in experiments and calculations to obtain the atomic data of low-charged tungsten ions, including ionization cross sections and spectra lines [4–44]. When studying the ionization cross sections [7,11] and spectra [4,5,33,39] of tungsten ions experimentally, ionization phenomena at energies far below the ionization potentials of corresponding ions were observed. To explain these phenomena, ionization contributions from metastable states have been proposed [5,7,11,13,33,45,46], whereas their influence on the charge-state evolution of tungsten ions in a plasma environment and the corresponding ionization mechanism have not yet been completely analyzed. Such ionizations from metastable levels could be important in the radiative cooling model in edge plasma.

Stenke *et al.* [7] measured the electron-impact single-ionization cross sections for $W^{q+}(q = 1$–$10)$ employing an electron-cyclotron-resonance (ECR) ion source, and calculated the electron-impact direct ionization (DI) cross sections using the Lotz formula. The calculated results were in reasonable agreement with the experimental data at high electron-impact energies (several times the ionization potential), but

strongly underestimated them at low energies. This indicated significant excitation-autoionization (EA) contributions from the ions. Moreover, the nonvanishing ionization signals below the ground-state ionization potentials of $W^{q+}(q = 4$–$10)$ were measured, which indicated significant DI + EA contributions from the metastable ions in the ion beams. Taking the DI and EA processes into account, configuration-average distorted-wave (CADW) approximations for the cross sections for the ground states of $W^{4+}$, $W^{5+}$, and $W^{6+}$ were carried out by Pindzola *et al.* [13]. The results for $W^{4+}$ and $W^{5+}$ fitted well with the experiments [7] at energies above the ground-state ionization potentials; the ionization of $W^{6+}$ was found to be dominated by metastable ions (~40 eV); but the ionization signals for $W^{5+}$ and $W^{6+}$ at energies far below the ionization potentials were not completely explicated in the paper. Detailed level-to-level distorted-wave calculations and more complete cross-section experiments for $W^{5+}$ were reported by Jonauskas *et al.* [11]. The calculations, employing the flexible atomic code (FAC) [19], were used to investigate the DI + EA cross sections for the levels in the ground configuration $4f^{14}5s^25p^65d$ and the metastable levels in the excited configurations $5p^55d^2$ and $4f^{13}5d^2$. And, the correlation effect on DI + EA processes was included for the ground configuration using the configuration interaction (CI) method, but excluded for the metastable levels in the excited configurations due to limitations in computing resources. The $W^{5+}$ effective ionization cross section [11], which was the weighted summation of the cross sections for the ground levels and metastable levels, agreed well with all the experimental data [11]. For $W^{6+}$, its ionization mechanism remained to be studied.

In the experiments employing electron-beam ion traps (EBITs), the spectral lines from $W^{6+}$, $W^{7+}$, and $W^{8+}$ have been observed when the electron energies are far below the ionization potentials of $W^{5+}$, $W^{6+}$, and $W^{7+}$,

───────
[*]xiao_jun@fudan.edu.cn

respectively [4,5,33,39]. Mita *et al.* [5] pointed out that metastable levels ($\sim$40 eV) might account for the inconsistency, in which the ionization threshold of $W^{6+}$ decreases from 122 to $\sim$80 eV. However, Lu *et al.* [33] observed the ionization of $W^{6+}$ at $\sim$50 eV, and proposed a hypothesis in which the ground-state ions of $W^{6+}$ would be excited to metastable levels ($\sim$40 and $\sim$85 eV) step by step before finally being ionized. The works above for $W^{5+}$, $W^{6+}$, and $W^{7+}$ indicate that metastable levels probably play important roles in the ionization of low-charged tungsten ions in a plasma environment.

A level-to-level collisional-radiative model (CRM) involving multiple charge states can quantitatively represent the level populations, line intensities, and ionization-recombination balance considering the influences of metastable levels. It can be utilized to study the charge-state evolution of tungsten ions and confirm the indirect ionization hypothesis for $W^{6+}$ in Ref. [33]. Detailed CRM studies involving multiple, highly charged ions and employing the non-Maxwellian collisional-radiative code NOMAD have been reported [46,47]. However, a multicharge-state CRM that considers a large contribution from EA processes has not been reported for such a complicated system as a $4f$ open shell yet.

In this work, various atomic data of $W^{5+}$, $W^{6+}$, and $W^{7+}$ with CI effects, involving (de)excitation, ionization, and recombination, are calculated using the FAC. In particular, the DI + EA cross sections are investigated for the metastable levels of $W^{5+}$ and $W^{6+}$. The data are imported to the CRM module implemented in the FAC to perform multicharge-state CRM simulations. For comparison, the visible and extreme ultraviolet (EUV) spectra of $W^{5+}$, $W^{6+}$, and $W^{7+}$ are measured using the high-temperature superconducting electron-beam ion trap (SH-HtscEBIT) [48].

## II. EXPERIMENT

The SH-HtscEBIT is designed for spectroscopic studies of tokamak edge plasmas [48]. A brief introduction is given here, but more detailed descriptions can be found in previous works [29–35]. The SH-HtscEBIT emits an electron beam from a cathode. The electron beam is focused by a magnetic field created by a pair of superconducting coils and travels through three drift tubes (DT1, DT2, and DT3). In drift tube DT2, atoms injected by an injection system are ionized and excited by the electron beam, whose energy depends on the potential difference between the cathode and DT2. The ions are trapped axially by a potential well ($\sim$100 V) created by DT1 and DT3, and radially by the magnetic field and the space-charge field of the electron beam (estimated to be less than 10 V). The ion temperature is strongly affected by the axial potential and radial potential [49,50].

The top-view diagram of the experimental setup is shown in Fig. 1. Light emitted from the ions is recorded by two spectrometers. One is a grazing-incidence flat-field spectrometer for EUV spectra ranging 17–25 nm, and the other is an Andor Czerny–Turner spectrometer for visible spectra ranging 560–620 nm. $W(CO)_6$ is injected into the space inside the drift tubes through the injector. The injection pressure is maintained at $1.5 \times 10^{-7}$ Torr and the background vacuum
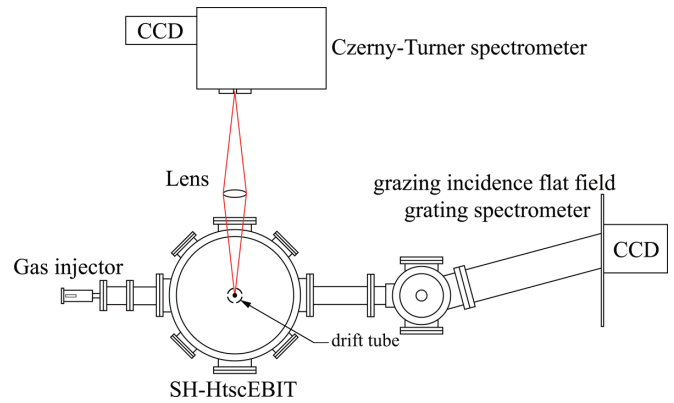


FIG. 1. Top-view diagram of the experimental setup in the present measurements. The direction of the electron beam traveling through the drift tube is out of the page.

pressure at $8 \times 10^{-10}$ Torr. Nominal electron-beam energies are set at 56, 58, 68, 78, 88, and 98 eV with current emission at 2 mA to obtain the spectra from $W^{5+}$ to $W^{7+}$. Considering the output deviations of power supplies and the space-charge effect from electron beam and ion cloud [33], the corrected electron-beam energies are 48, 50, 60, 70, 80, and 90 eV, respectively, with uncertainties estimated to be less than 5 eV.

## III. CALCULATIONS

In this work, the relativistic CI method implemented in the FAC is used. Atomic data, including energy levels, level-to-level cross sections for electron-impact DI, collisional excitation (CE), radiative recombination (RR), charge exchange (CX), and level-to-level decay rates for radiative transition (RT) and autoionization (AI), are calculated for the ions of interest. The DI + EA cross sections for metastable levels are investigated, where EA is a composite process of CE and AI. All the data are calculated using two models to study the influence of CI on the calculations. In model 1, only the CI effect within the same nonrelativistic configuration (intraconfiguration interaction) is considered. In model 2, besides intraconfiguration interaction, the CI effect among different nonrelativistic configurations (interconfiguration interaction) is also considered, whereas the number of the energy levels named "CI scale" is limited by computing resources. Multicharge-state CRM simulations using the calculated data from the two models are performed.

### A. Energy levels

In the atomic structure calculations, the ground configuration of each ion is taken for the optimization of central potential of that ion. The central potential of the lower charge-state ion is used to calculate the ionization and recombination processes.

For $W^{5+}$, the configurations of the primary metastable levels are $5p^5 5d^2$ and $4f^{13} 5d^2$. For $W^{6+}$, in addition to the configurations $4f^{13} 5d$, $5p^5 5d$ ($\sim$40 eV) and $4f^{13} 5p^5 5d^2$ ($\sim$85 eV) mentioned in Ref. [33], $4f^{12} 5d^2$ ($\sim$85 eV) is an important configuration with metastable levels. Considering the different atomic processes

TABLE I. Main configurations introduced in the calculations, including the configurations in bold and their single excitations. $n \leqslant a(a')$, $l \leqslant b(b')$ means that excitations to principal quantum numbers $n \leqslant a$ and orbital quantum numbers $l \leqslant b$ are included in both calculation models, and excitations to $n \leqslant a'$, $l \leqslant b'$ (and their parent configurations in bold) participate in the interconfiguration interaction in model 2. To show the excitations clearly, some are repeated in the table, but taken only once in the calculations. For example, the excitations of $5d$ from $4f^{13}5d^2$ and $4f$ from $4f^{14}5s^25p^65d$ contain repeated configurations.

| Ion | Configuration | Excitation |
|---|---|---|
| W$^{5+}$ | $\mathbf{4f^{14}5s^25p^65d}$ | $4f, 5s, 5p, 5d \rightarrow n \leqslant 8(8),$ $l \leqslant 4(4)$ |
| | $\mathbf{5p^55d^2}$ and $\mathbf{4f^{13}5d^2}$ | $5d \rightarrow n \leqslant 8(8),\ l \leqslant 4(4)$ |
| | | $4f, 5p \rightarrow n \leqslant 9(6),\ l \leqslant 3(3)$ |
| | | $5s \rightarrow n \leqslant 6(5),\ l \leqslant 3(3)$ |
| W$^{6+}$ | $\mathbf{5p^6}$ | $4f, 5s, 5p \rightarrow n \leqslant 7(7),\ l \leqslant 3(3)$ |
| | $\mathbf{4f^{13}5d}$ and $\mathbf{5p^55d}$ | $4f, 5p, 5d \rightarrow n \leqslant 7(7),\ l \leqslant 3(3)$ |
| | | $5s \rightarrow n \leqslant 6(6),\ l \leqslant 3(3)$ |
| | $\mathbf{4f^{12}5d^2}$ and $\mathbf{4f^{13}5p^55d^2}$ | $5d \rightarrow n \leqslant 7(7),\ l \leqslant 3(3)$ |
| | | $4f, 5p \rightarrow n \leqslant 6,\ l \leqslant 3(5d)$ |
| | | $5s \rightarrow 5d(5d)$ |
| W$^{7+}$ | $\mathbf{4f^{13}}$ and $\mathbf{5p^5}$ | $4f, 5s, 5p \rightarrow n \leqslant 6(6),\ l \leqslant 3(3)$ |
| | $\mathbf{4f^{13}5p^55d}$ | $5d \rightarrow n \leqslant 6(6),\ l \leqslant 3(3)$ |
| | | $4f, 5s, 5p \rightarrow 5d,\ 5f(5d, 5f)$ |
| | $\mathbf{4f^{11}5d^2}$ | |
| | $\mathbf{4f^{12}5s5d^2}$ | |

from these metastable levels, the primary configuration setup is given in Table I. In total, 189 741 levels of W$^{5+}$, 267 793 levels of W$^{6+}$, and 8458 levels of W$^{7+}$ are included in the calculations.

It should be noted that when studying the ionization from W$^{5+}$ to W$^{6+}$, to save computing resources, the W$^{6+}$ configurations setup is downsized to include mainly the configurations $5p^6$, $4f^{13}5d$, $5p^55d$, and their excitations to $n = 5$, $l \leqslant 3$; i.e., a smaller CI scale for W$^{6+}$.

## B. Ionization cross sections

In this work, electric-dipole (E1) and quadrupole (E2), as well as magnetic-dipole (M1) and quadrupole (M2) transitions are considered for nonautoionizing levels. At electron energies of 48–90 eV (electron velocities $\sim 5 \times 10^8$ cm/s), the electron-ion collision cross sections (mainly contributed from CE cross sections) for the levels in our configurations of interest are several $10^{-16}$ cm$^2$ [13]. With the electron densities of $\sim 2 \times 10^{10}$ cm$^{-3}$ in our experiments, the corresponding

collision rates are several $10^3$ s$^{-1}$. Thus, the collision processes are considerable for the levels whose lifetimes exceed $10^{-5}$ s as a conservative estimate. These levels are regarded as metastable levels, and their respective total ionization cross sections $\sigma_i^{TOT}$ are investigated:

$$\sigma_i^{TOT} = \sum_j \sigma_{ij}^{DI}(E_e) + \sum_{k>i} \sigma_{ik}^{CE}(E_e)B_k, \qquad (1)$$

where $\sigma_{ij}^{DI}(E_e)$ is the DI cross section from level $i$ of W$^{q+}$ to level $j$ of W$^{(q+1)+}$ at electron energy $E_e$, $\sigma_{ik}^{CE}$ is the CE cross section of W$^{q+}$ from level $i$ to $k$, and $B_k$ is the AI branching ratio of level $k$. $\sigma_{ik}^{CE}(E_e)B_k$ refers to the EA process. $B_k$ can be expressed as

$$B_k = \frac{\sum_j A_{kj}^{AI} + \sum_{n<k} A_{kn}^{RT}B_n}{\sum_j A_{kj}^{AI} + \sum_{n<k} A_{kn}^{RT}}, \qquad (2)$$

where $A_{kj}^{AI}$ is the AI rate from level $k$ of W$^{q+}$ to level $j$ of W$^{(q+1)+}$, and $A_{kn}^{RT}$ is the RT rate of W$^{q+}$ from level $k$ to $n$.

According to Eqs. (1) and (2), the exact result for the EA cross section for level $i$ requires extremely large-scale calculations for the RT process among more than 100 000 levels. As a roughly competitive relationship between AI and RT in $B_k$, the calculated AI rates for most autoionizing levels in this work are much larger than their RT rates (generally $< 10^{12}$ s$^{-1}$ for E1 transitions), so the calculation is simplified via the following procedure. All the AI rate data are first obtained, and the E1 transitions from an autoionizing level are calculated only if the total AI rate of this level is less than $10^{12}$ s$^{-1}$. Then, the M1 + E2 transitions from an autoionizing level are calculated only if the total AI + RT (E1) rates of this level are less than $10^6$ s$^{-1}$. This simplification increases the EA cross sections by 0–3% in the calculation.

## C. Multicharge-state CRM simulation

The CRM describes the steady-state equilibriums of levels in different atomic processes. The RT, AI, DI, RR, CX, CE, and collisional deexcitation (DE) processes are considered in the present multicharge-state CRM simulation. For dielectronic recombination (DR), according to Kwon's result [51] and our calculations using configuration-average approximation, the energies required for the strong resonance processes for ground levels of W$^{6+}$ and W$^{7+}$ are lower than our selected electron energies with narrow Gaussian distribution. The case of $4f^{13}5d$ which has very large metastable fraction is the same. Hence, DR is neglected in our CRMs. As results, small deviations on the abundance fractions of different ions ($<0.04$) may occur in the simulations for 48 and 50 eV, but the influences are negligible for higher energies where the CX is stronger than DR by orders. The balanced equation of level population is

$$\frac{dN_i}{dt} = \sum_{k>i}\left(A_{ki}^{RT}N_k\right) + \sum_h\left(A_{hi}^{AI}N_h\right) - \sum_{k<i}\left(A_{ik}^{RT}N_i\right) - \sum_j\left(A_{ij}^{AI}N_i\right) + \left[\sum_{k<i}\left(C_{ki}^{CE}N_k\right) + \sum_{k>i}\left(C_{ki}^{DE}N_k\right) + \sum_h\left(C_{hi}^{DI}N_h\right) + \sum_j\left(C_{ji}^{RR}N_j\right)\right]n_e$$

$$- \left[\sum_{k>i}\left(C_{ik}^{CE}N_i\right) + \sum_{k<i}\left(C_{ik}^{DE}N_i\right) + \sum_j\left(C_{ij}^{DI}N_i\right) + \sum_h\left(C_{ih}^{RR}N_i\right)\right]n_e + \sum_j\left(C_{ji}^{CX}N_j\right)n_{cx} - \sum_h\left(C_{ih}^{CX}N_i\right)n_{cx} = 0, \qquad (3)$$

where $N_i$ and $N_k$ are the populations of level $i$ and $k$ of $W^{q+}$, respectively. $h$ and $j$ are the energy levels of $W^{(q-1)+}$ and $W^{(q+1)+}$, respectively. $C^{CE}$, $C^{DE}$, $C^{DI}$, and $C^{RR}$ are the rate coefficients for the CE, DE, DI, and RR processes obtained by convoluting the corresponding cross sections with the Gaussian-distribution electron-collision energy function. The DE cross section is calculated according to the detailed balance principle. $C^{CX}$ is the CX rate coefficient obtained by convoluting the CX cross section with the Maxwellian-distribution CX-collision-energy function depending on ion temperature. $n_e$ is the electron density, and $n_{cx}$ is the CX neutral-target density. The population of each level can be obtained by Eq. (3) with the normalization condition $\sum_{h,i,j...} N_{h,i,j...} = 1$.

The electron density $n_e$ considering the overlap factor [52,53] is estimated to be about $2.2 \times 10^{10}$ cm$^{-3}$ at 230 eV with a current of 6.8 mA by measuring the widths of the electron beam and ion beam. Then $n_e$ is corrected according to the energies and current set in the experiments before being adopted in the CRM. The ion temperature is estimated according to 1/3 of the radial potential, i.e., 18–24 eV, depending on the electron energy. The density $n_{cx}$ is taken as $10^{10}$ cm$^{-3}$, which is an estimated value converted from the injection pressure using the ideal gas law. The neutral targets are set as $N_2$ and $H_2$ separately. Due to the uncertainties of the CX cross section and the density $n_{cx}$, the CX process is regarded as a large error source in the simulations. The CX process is mainly used to provide strong recombination channels, as the RR process is weak in the present calculations.

To save on computing resources, the simplification of the RT process in Sec. III B is also adopted in the CRM. Similarly, since the particle impact processes (CE, DE, DI, RR, and CX) are much slower than the decay processes (RT, AI) for most levels in our CRM with low particle densities, the particle impact processes from a level are calculated only if the AI + RT rates of this level are less than $10^7$ s$^{-1}$. These two simplifications affect the population results by less than 1%. To avoid extremely slow convergence, the high-orbit configurations, for which the interconfiguration interaction is not considered in model 2, are not introduced into the CRM, which influences the simulations

negligibly at energies below 90 eV. Nevertheless, the FAC code is optimized with 8-bit integer promotion and multi-threading basic linear algebra subprograms (BLAS) library to allow a large-scale CRM simulation involving 103 351 levels.

## IV. RESULTS AND DISCUSSION

### A. Energy levels and ionization cross sections

The ionization potentials of the ground levels and the energies of the metastable levels of $W^{5+}$ and $W^{6+}$ are shown in Table II. The ionization potentials in model 2 are closer to the NIST data [54] (with energy differences less than 1.5 eV) than those in model 1. The energy discrepancies between the present calculations and the NIST data are large for some of the excited-metastable levels, mainly due to the optimization of the central potential and the CI scale. The energy of the first excited level of $W^{6+}$ $(4f_{7/2}^{13}5d_{3/2})_2$ is 38.6 eV in NIST [24,42,54], while in model 1 it is 35.4 eV, and in model 2, 29.0 eV with a large CI scale, but 37.4 eV with a small CI scale. However, the data of $5p^55d$ levels in the two models are both close to the NIST data, e.g., the energies differ by about 1 eV for $(5p_{1/2}^55d_{3/2})_1$, the upper level of the strong E1 transition to $5p^6$ at 21.62 nm [24]. This is the smallest deviation among different central potential selections. Since the energy discrepancies are much smaller for the intraconfigurational level intervals than the interconfigurational ones, the M1 transitions are more accurate than the E1 transitions in this work. Except for $5p^55d^2$ and $5p^55d$, the average energies of the metastable levels of interest vary by about 5 eV after a large CI scale is considered. Strong mixing occurs among the configurations. For convenience, the metastable levels in model 2 are labeled by their leading configurations.

The DI + EA cross sections for the metastable levels in $4f^{13}5d^2$ and $5p^55d^2$ of $W^{5+}$, and in $4f^{12}5d^2$ and $4f^{13}5p^55d^2$ of $W^{6+}$ are shown in Fig. 2, where the EA cross sections dominate. For $W^{5+}$, the results of $4f^{13}5d^2$ and $5p^55d^2$ in model 1 are in good agreement with the data given by Jonauskas [11]. Generally, the cross sections for most levels in model 2

TABLE II. Ionization potentials of the ground levels, and energies of the metastable levels of $W^{5+}$ and $W^{6+}$. The labels "m1" and "m2" refer to the results obtained employing model 1 and model 2, respectively. The "MCDF" refers to the multiconfigurational Dirac–Fock method [7]. The numbers in parentheses refer to the numbers of the metastable levels whose lifetimes exceed $10^{-5}$ s.

| | | Ionization potentials (eV) | | | | Level energy (eV) | |
|---|---|---|---|---|---|---|---|
| Ion | Configuration | FAC$^{m1}$ | FAC$^{m2}$ | MCDF [7] | NIST [54] | FAC$^{m1}$ | FAC$^{m2}$ |
| $W^{5+}$ | $5d$ | 63.5 | 63.9 | 63.58 | 64.77 | 0 | 0 |
| | $4f^{13}5d^2$ | | | | | 34.0–40.7(30) | 30.6–37.2(30) |
| | $5p^55d^2$ | | | | | 39.0–53.3(7) | 40.3–54.0(7) |
| $W^{6+}$ | $5p^6$ | 118.3 | 120.7 | 119.0 | 122.01 | 0 | 0 |
| | $4f^{13}5d$ | | | | | 35.4–40.5(17) | 29.0–33.9(17) |
| | $4f^{13}5d^a$ | | | | | 35.4–40.5(17) | 37.4–42.7(17) |
| | $5p^55d$ | | | | | 37.6–52.5(9) | 38.5–52.7(9) |
| | $4f^{12}5d^2$ | | | | | 79.4–92.8(34) | 84.1–95.9(33) |
| | $4f^{13}5p^55d^2$ | | | | | 78.6–93.8(13) | 83.0–98.5(12) |

[a] The levels of $W^{6+}$ acting as free states when studying the ionization cross sections for $W^{5+}$; i.e., calculated with a smaller CI scale.
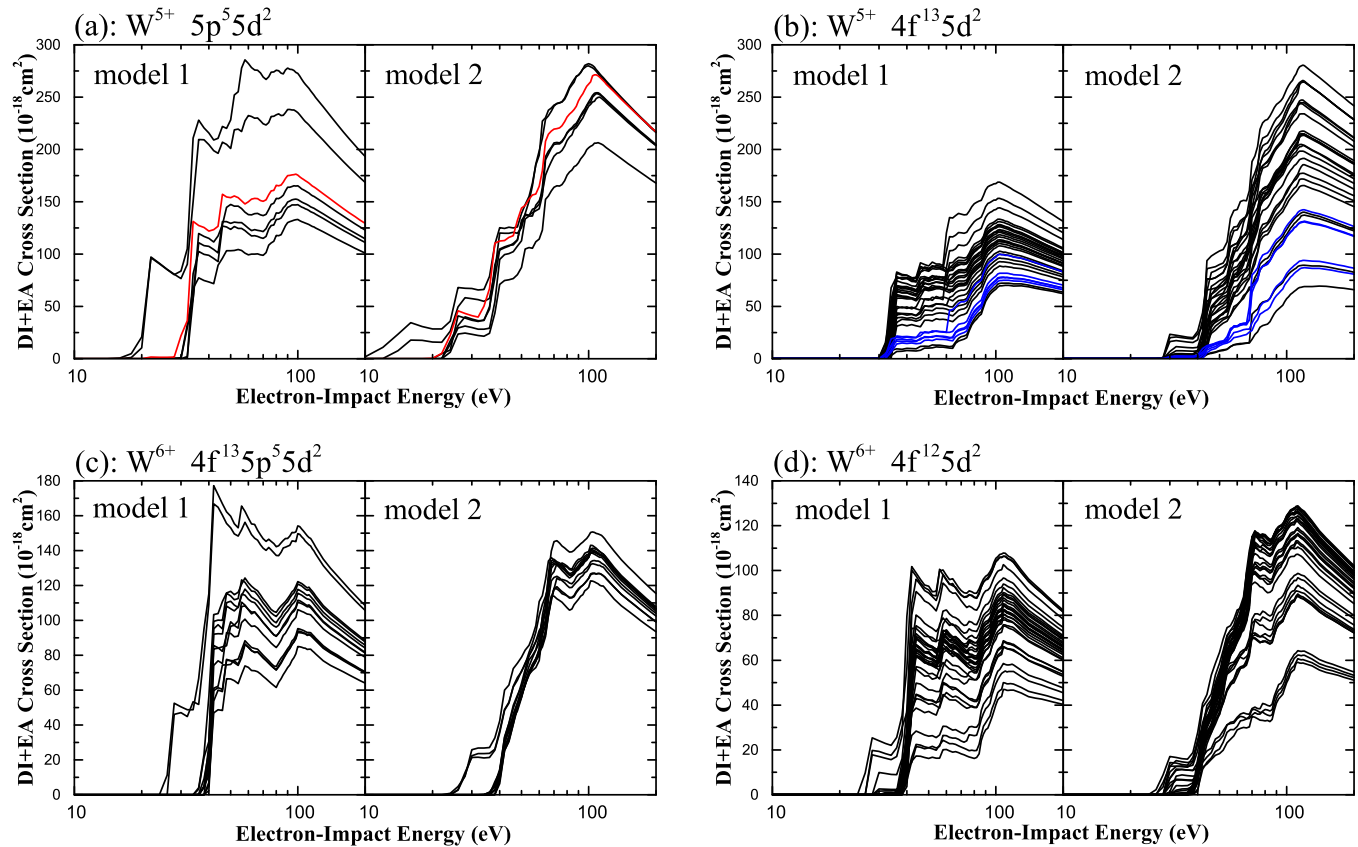
FIG. 2. DI + EA cross sections for the metastable levels in $5p^55d^2$, $4f^{13}5d^2$, $4f^{13}5p^55d^2$, and $4f^{12}5d^2$ which are shown in panels (a), (b), (c), and (d), respectively. In each panel, the results calculated using model 1 and model 2 are both given. The red lines in (a) represent the results for the $5p^55d^2$ level which is corresponding to level No. 105 in Ref. [11]. The blue lines in (b) represent the results for the $4f^{13}5d^2$ levels whose angular momentums $j$ are 13/2. These levels do not mix with $5p^55d^2$, as the largest value of $j$ for $5p^55d^2$ is 11/2.

become smaller at low energy, but larger at peak than those in model 1. The calculated cross sections are greatly affected by the interconfiguration interaction. One reason is the energy discrepancy between two models, which can shift the cross-section curves and make some level-to-level channels become energetically allowed or forbidden. For instance, in Fig. 2(a), the difference of the cross sections for $5p^55d^2$ at energies below 20 eV between the two models results from newly allowed Auger channels. Another reason is configuration mixing, which is largely responsible for the increase in the peak value of the cross sections. To explain the influence of the configuration mixing, the EA process from the $5p^55d^2$ level marked in red in Fig. 2(a), whose leading configuration is $[(5p^5_{3/2}5d_{3/2})_25d_{5/2}]_{9/2}$, is analyzed using the two models as a typical case of those from the considered metastable levels.

The largest four CE channels from the $[(5p^5_{3/2}5d_{3/2})_25d_{5/2}]_{9/2}$ level to the autoionizing configurations using model 1 are shown in Fig. 3. The level structure is also partly given in Fig. 4. The CE process from the $5p^55d^2$ level is dominated by $5d$–$5f$, $5d$–$6p$, $5p$–$5d$, and $4f$–$5d$ excitations. For the $5d$ excitations to $5f$ and $6p$, one of the final configurations $5p^55d5f$ mainly decays to $5p^6$ of W$^{6+}$ via the Auger process, but such Auger decays to $5p^6$ are partly forbidden energetically for $5p^55d6p$. For the $5p$–$5d$ excitation, $5p^45d^3$ has no normal Auger decay to $5p^6$ despite its higher energies, and its Auger decays to $5p^55d$

are also partly forbidden energetically. The case of $4f$–$5d$ excitation is similar to that of $5p$–$5d$ excitation. Finally, only the $5d$–$5f$ excitation has large EA contribution in the four excitations.

In model 2, the interconfiguration interaction is considered, leading to configuration mixing. The CE cross section to a specific configuration becomes meaningless, and the total CE cross sections to autoionizing configurations decrease for most metastable levels; the Auger channels from some autoionizing configurations are "extended": For $5p^45d^3$, used as a simplified example in Fig. 4, its decays to $5p^6$ are allowed due to its mixing with $5p^55d5f$, and its decays to $4f^{13}5d$ are also partly allowed due to the mixing between $5p^55d$ and $4f^{13}5d$. That is, $5p^45d^3$, to which the excitations are strong, also contributes to the EA cross sections considerably due to the indirectly extended Auger channels. The case of other autoionizing configurations, such as $4f^{14-N}5p^{4+N}5d^3$ of W$^{5+}$ and $4f^{13-N}5p^{4+N}5d^3$ of W$^{6+}$ is similar. When no CI is included, there is no mixing as the Hamiltonian is assumed to be diagonal; the channel from one pure state to another is strict. The CI effect "redistributes" the channel to different energy levels and reduces the restrictions. In model 2, generally, the energy shift for levels, the loss on the CE channels (to autoionizing levels), and the compensation from larger Auger channels result in changes in the EA cross sections.
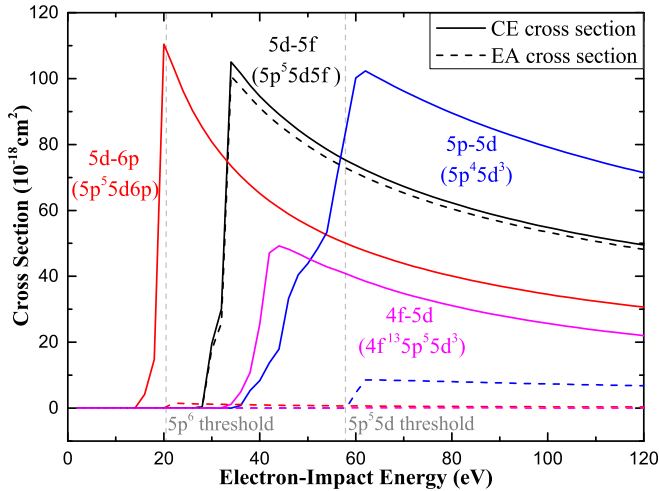
FIG. 3. CE cross sections for the $5d$–$5f$ (black), $5d$–$6p$ (red), $5p$–$5d$ (blue), and $4f$–$5d$ (magenta) excitations from $[(5p^5_{3/2}5d_{3/2})_2 5d_{5/2}]_{9/2}$ and the four corresponding EA cross sections employing model 1. The configurations in the parentheses are the final configurations of the corresponding excitations. The solid lines and the dashed lines represent the CE cross sections and the EA cross sections, respectively.

The DI + EA cross sections for the $W^{6+}$ metastable levels in $4f^{13}5d$ and $5p^5 5d$ were also investigated and found to be qualitatively similar to each other. The results for the $W^{6+}$ ground-level $5p^6$ and longest-lifetime excited level $(4f^{13}_{7/2}5d_{3/2})_5$ are shown in Fig. 5. All the theories, including our calculations and the CADW calculations by Pindzola and Griffin [13], disagree with the experimental data [7]. One reason is the uncertainties in the calculations. In addition, it can be seen that the experimental data rise slightly at energy of
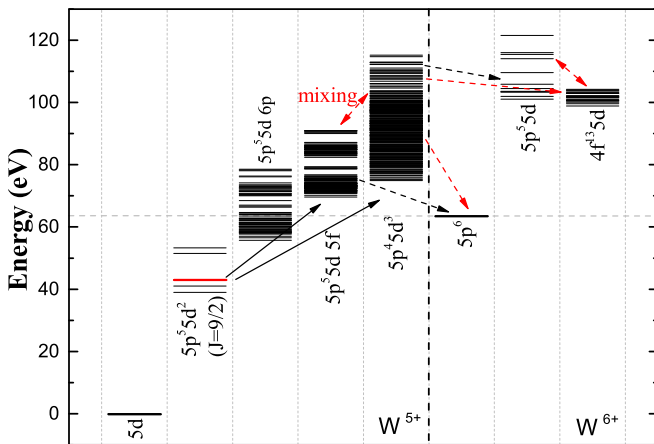


FIG. 4. Energy levels involved in the EA process of $5p^5 5d^2$. Only part of configurations are shown as a simplified example. The energy level marked in red is $[(5p^5_{3/2}5d_{3/2})_2 5d_{5/2}]_{9/2}$. The solid arrows represent the CE process. The dashed arrows (black) represent the AI process when only the intraconfiguration interaction is introduced. The dashed arrows (red) represent the extra Auger channels allowed indirectly when the interconfiguration interaction is introduced, and the double-dashed arrows (red) represent mixing among the configurations.
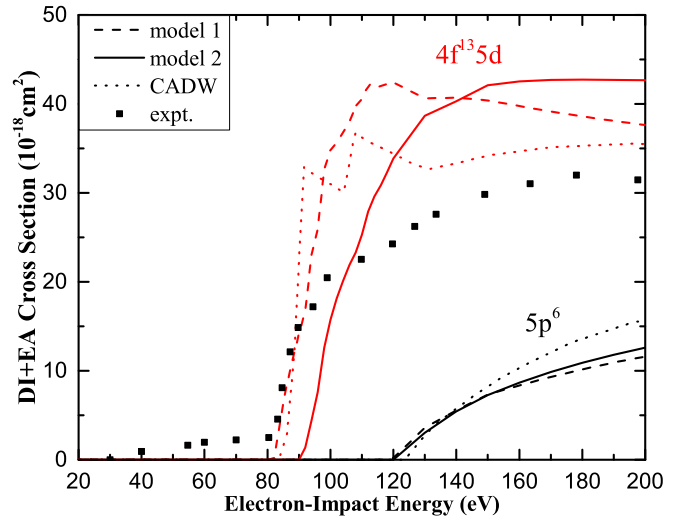


FIG. 5. DI + EA cross sections for $W^{6+}$. The dots represent the experimental data [7]. Theoretical results for the ground level $5p^6$ (black) and excited level $(4f^{13}_{7/2}5d_{3/2})_5$ (red) are given for three methods: The dashed lines and the solid lines represent the FAC results using model 1 and model 2, respectively; the dotted lines represent the CADW results [13].

$\sim 40$ eV, and rapidly at energies above 80 eV, which are much lower than the ionization potential of 122 eV. That is, the experimental data are not contributed from an individual level, but from the mixture of ground- and metastable levels, which is the other reason for the disagreements. The steep rises in the cross-section curves for $(4f^{13}_{7/2}5d_{3/2})_5$ are close to the second rise in the experimental data at 80 eV despite the curve shift in model 2. Moreover, the corresponding peak values are larger by $\sim 30\%$ than those of the CADW calculations. It can be indicated that the $4f^{13}5d$ and $5p^5 5d$ metastable levels with large populations [5,33] can play important roles in the ionization of $W^{6+}$ at energies above 80 eV.

It should be noted that the interconfiguration interaction is only considered with $n \leqslant 8$ or less for the metastable levels and autoionizing levels. More configurations should be introduced in the CI scale to obtain more accurate cross-section results. However, the computing cost, especially for $4f^{12}5d^2$ and $4f^{13}5p^5 5d^2$, will increase explosively when more configurations with high orbits are included.

### B. Experiment and CRM simulation

Experimental spectra of $W^{5+}$, $W^{6+}$, and $W^{7+}$ for the EUV and visible ranges are given in Fig. 6(a) and 6(b), respectively. In Fig. 6(b), the spectral line at 574.47 nm is identified as the $W^{7+}$ M1 transition between $4f^{13}_{7/2}$ and $4f^{13}_{5/2}$, as reported in Refs. [33,39]. The line begins to appear at about 48 eV, indicating the ionizations of $W^{5+}$ and $W^{6+}$ at energies far below their ionization potentials of 65 and 122 eV, respectively. The strength of the line is close to maximum at 60 eV. That is, the $W^{7+}$ ions begin to populate at 48 eV and have a large population at 60 eV. In Fig. 6(a), the EUV spectrum at 48 eV shows nothing since the energy is not enough for the E1 transition at that wavelength band. The spectral line at
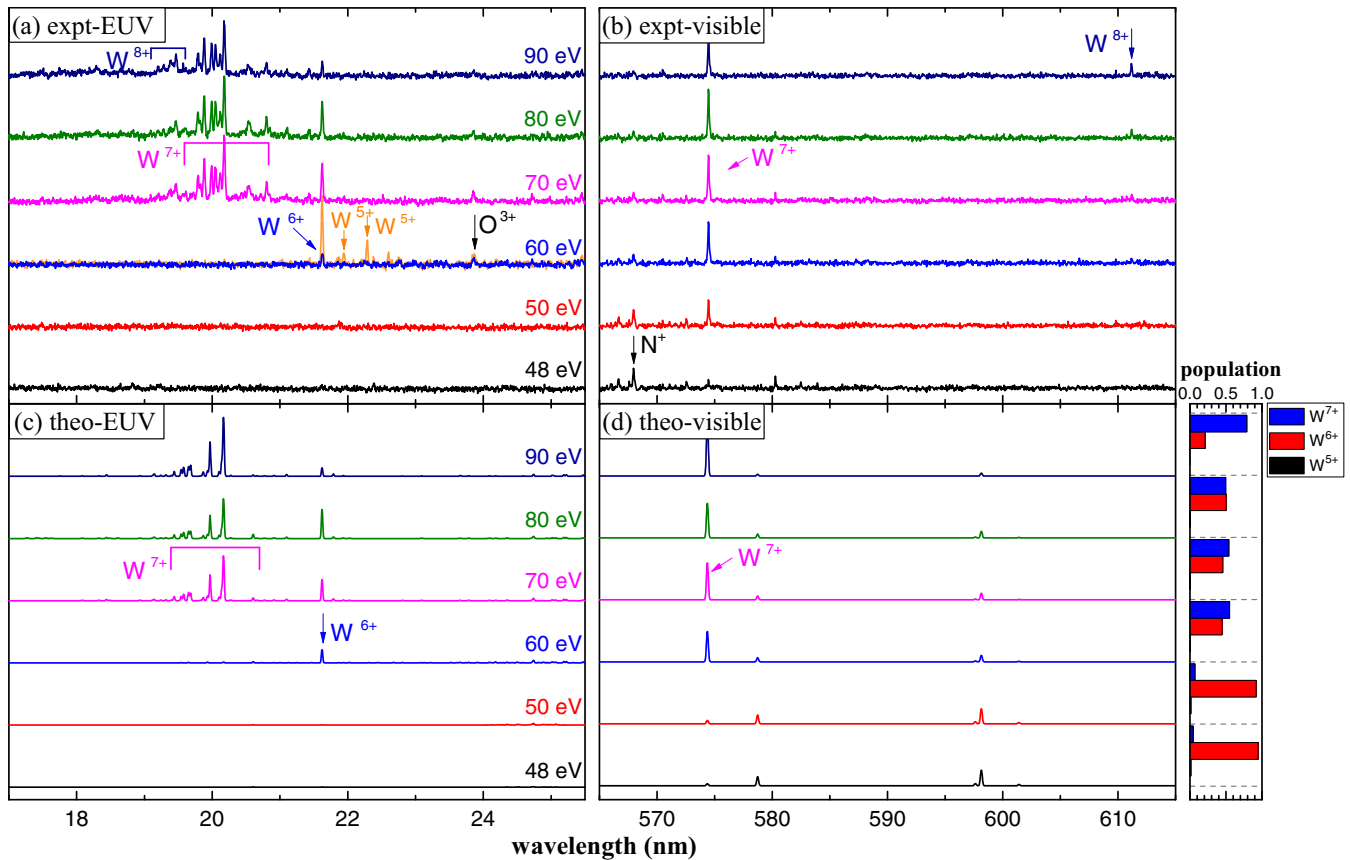
FIG. 6. Experimental spectra (a), (b) and multicharge-state CRM simulated spectra (c), (d) in the ranges of 17–25 nm and 560–620 nm for W at 48–90 eV. For experimental spectra (a) and (b), the electron-beam energies shown in the right side of EUV panel are corrected values as mentioned in Sec. II. In (a), the orange spectrum at 60 eV is the remeasured result with 10 times the original injection pressure. The wavelengths of the spectral lines in the simulated spectra (c) and (d) are shifted. The simulated results of the ion populations at different energies are shown in the bar graph.

21.62 nm (57.4 eV) appears at 60 eV, which is identified as the W$^{6+}$ E1 transition measured by Sugar and Kaufman [24]. This W$^{6+}$ line becomes strongest at 70 eV, indicating that the W$^{6+}$ ions still have a considerable population at 70 eV, though the W$^{7+}$ ions have largely populated. And, the W$^{7+}$ transition array at around 20 nm (~62 eV), mainly including 5$p$–5$d$, 5$p$–6$s$, and 4$f$–5$d$ transitions [4,5,33,39], appears after the energy exceeds 60 eV. The spectral shape changes little as the energy increases from 60 to 80 eV, except for the EUV spectrum at 60 eV. It can be inferred that the populations of W$^{6+}$ and W$^{7+}$ ions are roughly unchanged at 60–80 eV. When the energy reaches 90 eV, the intensity of the W$^{6+}$ line at 21.62 nm decreases significantly. The W$^{8+}$ line at 611.18 nm and the array at around 19.2 nm [5,34,40] become strong. Moreover, the spectral lines from W$^{5+}$ at 21.9–22.3 nm identified by Clementson [4] are not found throughout the energy increase. The spectrum at 60 eV is measured again at 10 times the original injection pressure and represented in orange in Fig. 6(a), in which the marked lines rising clearly at 21.94 and 22.29 nm are identified as the two strongest W$^{5+}$ lines reported in Ref. [4]. The W$^{5+}$ lines do not appear along with the strong W$^{6+}$ line at 70 eV, where the requirement for the transition energy is satisfied. It can be inferred that with low injection pressure, the population of W$^{5+}$ ions is probably

not that large at 60 eV, and rather small when the energy is above 60 eV.

The CRM simulated spectra corresponding to our experiments, which employ the data calculated in model 2 and set N$_2$ as the neutral target, are shown in Fig. 6(c) and 6(d). The population results of different ions are given at the right side of Fig. 6(d). To match the experimental spectra, some of the theoretical spectral lines are shifted: that is, by 0.4 nm for the W$^{6+}$ lines at 21.62 nm, ~1.2 nm holistically for the W$^{7+}$ transition array in the EUV spectra, and 2.2 nm for the W$^{7+}$ line at 574.47 nm. A disagreement between the experimental and theoretical W$^{7+}$ transition array still exists after the shifting. Only the strongest line $(4f^{13}5p^6)_{7/2}$–$(4f^{13}5p^55d)_{9/2}$ at 20.17 nm [4] is matched with the experiments. Moreover, blending occurs in the theoretical array, e.g., the line $(4f^{13}5p^6)_{7/2}$–$(4f^{13}5p^55d)_{9/2}$ at 20.17 nm is blended with another strong line, making the line look even stronger and the array look sparser. As the experimental array agrees with the Refs. [4,5,33,39], the uncertainties of the transition energies and spectral intensities in the calculations are supposed to be responsible for this disagreement. The open 4$f$-hole system of W$^{7+}$ results in the difficulty in theoretical works. The calculations for transitions between opposite parity states have large uncertainties. The accuracy of calculations for W$^{7+}$ re-
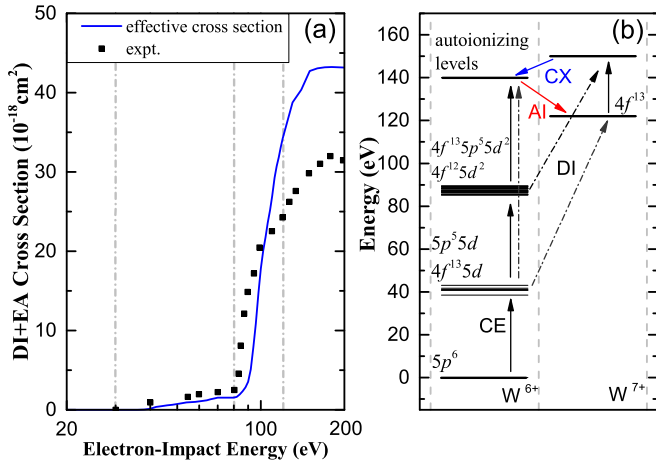
FIG. 7. (a) DI + EA cross sections for $W^{6+}$. The dots represent the experimental data [7]. The solid line (blue) represents the effective cross section for $W^{6+}$ (see text). (b) Ionization mechanism for $W^{6+}$. The solid lines represent the channels at about 50–80 eV. The dotted-dashed lines represent newly opened channels at about 80–120 eV.

mains to be improved. On the other hand, the population of $W^{5+}$ ions is less than $\sim 1\%$ for the entire energy range. At 48 and 50 eV, there are more than 92% $W^{6+}$ ions and less than 7% $W^{7+}$ ions, and the $W^{7+}$ line at 574.47 nm is observable. At 60–80 eV, the populations of $W^{6+}$ and $W^{7+}$ ions both maintain at about 50%, and their EUV lines appear. The population of $W^{7+}$ ions is dominant at 90 eV. The simulations are generally in agreement with our experiments, except that the population of $W^{5+}$ ions at low energy in the experiments is unclear. Simulations employing the data calculated in model 1, or setting $H_2$ as the neutral target were also performed, but no qualitative change in the spectra was found.

The present simulations reproduce the "abnormal" charge-state evolution for tungsten ions at extra-low energies found in our experiments. The effective DI + EA cross section for $W^{6+}$, which is the weighted summation of the cross sections for the long-lifetime levels, is given in Fig. 7(a). The weights are the populations of the levels taken from the simulation at 60 eV. The effective cross section has the same trend as the experimental data [7], and the distinctions of the two curves, including shift and stretch, are mainly caused by the uncertainties in our calculation and the differences in the metastable fractions between the ions extracted from the ECR ion source and the simulated EBIT plasma. According to the CRM simulations, the ionization mechanism for $W^{6+}$ at energies below the ionization potential is given in Fig. 7(b). When the energy is about 50–80 eV, the $W^{6+}$ ions at the ground level $5p^6$ can be excited to the metastable levels in $5p^55d$ and $4f^{13}5d$, and then further excited to the metastable levels in $4f^{13}5p^55d^2$ and $4f^{12}5d^2$, and finally ionized to $W^{7+}$ mainly through the EA processes of $4f^{13}5p^55d^2$ and $4f^{12}5d^2$. When the energy is about 80–120 eV, the ionization is dominated by the EA processes of the metastable ions in $5p^55d$ and $4f^{13}5d$. The present experiments and simulations show that at energies below 80 eV, though the fractions of the metastable ions in $4f^{13}5p^55d^2$ and $4f^{12}5d^2$ are small ($\sim 1\%$), the degree of ionization is still significant. As shown in Fig. 7(a), the

ionization signals at 30–80 eV measured in the cross-section experiments [7] arise from these metastable ions.

The ionization of $W^{5+}$ is similar to that of $W^{6+}$ but simpler. Our simulations show that the population of $W^{5+}$ is about 90% at 30 eV but decreases fast as the energy increases. Through EA processes, the metastable $W^{5+}$ ions in $5p^55d^2$ and $4f^{13}5d^2$ contribute to ionization significantly at energies above 30 eV which is much lower than the ionization potentials of $W^{5+}$ (64.77 eV) and even $W^{4+}$ (51.6 eV) [54]. Stenke *et al.*'s experiments [7] showed that the ionization threshold of $W^{4+}$ decreases to $\sim 40$ eV, which is possibly due to the metastable levels such as $5d6s\ ^1D_2$ at 9.05 eV [54]. After being ionized from $W^{4+}$ at $\sim 40$ eV, $W^{5+}$ will be quickly ionized indirectly to $W^{6+}$. Thus, the $W^{5+}$ ions would populate little if the recombination processes like CX and RR are relatively weak.

CRM simulations with an electron density of $10^{11}$ cm$^{-3}$ and a Maxwellian-distribution electron energy were also performed for the edge area of fusion devices which contains low-charged tungsten ions. The effective ionization (DI + EA) rate coefficients from our simulations and the recombination (DR + RR) rate coefficients by Preval *et al.* [55] were used to calculate the ionization balance from $W^{5+}$ to $W^{7+}$. We found that $W^{6+}$ and $W^{7+}$ ions are the most abundant at $\sim 70\%$ at temperatures of $\sim 17$ and $\sim 30$ eV, respectively, which are $\sim 5$ eV lower than the results by Preval *et al.* [55]. However, the metastable fractions change at different electron densities and temperatures, and metastable levels are not considered for the recombination rate coefficients [55]. The influence of metastable levels should be further studied.

## V. CONCLUSION

The charge-state evolution from the $W^{5+}$ to the $W^{7+}$ ions at energies below their ionization potentials was studied theoretically and experimentally. Level-to-level atomic data, including those of RT, AI, CE, DI, RR, and CX processes, were calculated using two CI methods. Theoretical DI + EA cross sections were studied for metastable levels of $W^{5+}$ and $W^{6+}$. Due to the interconfiguration interaction, the calculated DI + EA cross sections for the metastable levels in $5p^55d^2$ and $4f^{13}5d^2$ of $W^{5+}$, and $4f^{13}5p^55d^2$ and $4f^{12}5d^2$ of $W^{6+}$ decreased at energies below $\sim 60$ eV, but their peak values increased.

Multicharge-state CRM simulations using the calculated data were performed, and their results agreed with the experiments. The charge-state evolution below ionization potentials in EBIT plasma was reproduced theoretically. The $W^{5+}$ ions were strongly ionized to $W^{6+}$ ions at 35–60 eV due to the large EA contribution from the metastable ions in $5p^55d^2$ and $4f^{13}5d^2$. For $W^{6+}$, at energies of 50–80 eV, the metastable ions in $4f^{13}5p^55d^2$ and $4f^{12}5d^2$ could be enriched in population through a stepwise CE process, and then ionized to $W^{7+}$ through the EA process, resulting in a noticeable population fraction ($\sim 50\%$) of $W^{7+}$. And, these metastable ions are responsible for the ionization signal below 80 eV in the cross-section experiments [7]. When the energies were above 80 eV, the $W^{6+}$ ions were strongly ionized to the $W^{7+}$ ions, which could be attributed to the large DI + EA contribution from the metastable ions in $5p^55d$ and $4f^{13}5d$. For low-charged

tungsten ions in EBIT plasmas, metastable levels make an ionization contribution that cannot be ignored, and in fusion plasmas, they could render plasma radiative-cooling models more complicated as the ionization threshold decreases and the populations of the metastable levels fluctuate with electron temperature, density, and energy distribution.

[1] J. Clementson, P. Beiersdorfer, and T. Lennartsson, AIP Conf. Proc. **1525**, 78 (2013).

[2] T. Pütterich, R. Neu, R. Dux, A. D. Whiteford, M. G. O'Mullane, and ASDEX Upgrade Team, Plasma Phys. Controlled Fusion **50**, 085016 (2008).

[3] J. Horacek, J. Adamek, H. W. Müller, J. Seidl, A. H. Nielsen, V. Rohde, F. Mehlmann, C. Ionita, and E. Havlíčková, ASDEX Upgrade Team, Nucl. Fusion. **50**, 105001 (2010).

[4] J. Clementson, T. Lennartsson, and P. Beiersdorfer, Atoms **3**, 407 (2015).

[5] M. Mita, H. A. Sakauey, D. Kato, I. Murakami, and N. Nakamura, J. Phys. Conf. Ser. **875**, 012019 (2017).

[6] R. G. Montague and M. F. A. Harrison, J. Phys. B: At. Mol. Opt. Phys. **17**, 2707 (1984).

[7] M. Stenke, K. Aichele, D. Harthiramani, G. Hofmann, M. Steidl, R. Völpel, and E. Salzborn, J. Phys. B: At. Mol. Opt. Phys. **28**, 2711 (1995).

[8] J. Rausch, A. Becker, K. Spruck, J. Hellhund, A. Borovik, Jr., K. Huber, S. Schippers, and A. Müller, J. Phys. B: At. Mol. Opt. Phys. **44**, 165202 (2011).

[9] A. Borovik Jr., B. Ebinger, D. Schury, S. Schippers, and A. Müller, Phys. Rev. A **93**, 012708 (2016).

[10] D. Schury, A. Borovik Jr., B. Ebinger, F. Jin, K. Spruck, A. Müller, and S. Schippers, J. Phys. B: At. Mol. Opt. Phys. **53**, 015201 (2020).

[11] V. Jonauskas, A. Kynienė, S. Kučas, S. Pakalka, Š. Masys, A. Prancikevičius, A. Borovik, Jr., M. F. Gharaibeh, S. Schippers, and A. Müller, Phys. Rev. A **100**, 062701 (2019).

[12] M. Stenke, K. Aichele, D. Harthiramani, G. Hofmann, M. Steidl, R. Völpel, V. P. Shevelko, H. Tawara, and E. Salzborn, J. Phys. B: At. Mol. Opt. Phys. **28**, 4853 (1995).

[13] M. S. Pindzola and D. C. Griffin, Phys. Rev. A **56**, 1654 (1997).

[14] V. Jonauskas, S. Kučas, and R. Karazija, Lith. J. Phys. **49**, 415 (2009).

[15] D.-H. Zhang and D.-H. Kwon, J. Phys. B: At. Mol. Opt. Phys. **47**, 075202 (2014).

[16] D. Zhang, L. Xie, J. Jiang, Z. Wu, C. Dong, Y. Shi, and Y. Qu, Chin. Phys. B **27**, 053402 (2018).

[17] S. D. Loch, J. A. Ludlow, M. S. Pindzola, A. D. Whiteford, and D. C. Griffin, Phys. Rev. A **72**, 052716 (2005).

[18] F. Jin, A. Borovik, Jr., B. Ebinger, and S. Schippers, J. Phys. B: At. Mol. Opt. Phys. **53**, 075201 (2020).

[19] M. F. Gu, Can. J. Phys. **86**, 675 (2008).

[20] R. R. Kildiyarova, S. S. Churilov, Y. N. Joshi, and A. N. Ryabtsev, Phys. Scr. **53**, 454 (1996).

[21] F. G. Meijer, Physica (Amsterdam) **73**, 415 (1974).

[22] V. Kaufman and J. Sugar, J. Opt. Soc. Am. **66**, 1019 (1976).

[23] J. Sugar and V. Kaufman, J. Opt. Soc. Am. **69**, 141 (1979).

[24] J. Sugar and V. Kaufman, Phys. Rev. A **12**, 994 (1975).

[25] A. N. Ryabtsev, E. Y. Kononov, R. R. Kildiyarova, W.-Ü. L. Tchang-Brillet, and J.-F. Wyart, Opt. Spectrosc. **113**, 109 (2012).

[26] N. Ryabtsev, E. Y. Kononov, R. R. Kildiyarova, W.-Ü. L. Tchang-Brillet, and J.-F. Wyart, Phys. Scr. **87**, 045303 (2013).

[27] J.-F. Wyart, V. Kaufman, and J. Sugar, Phys. Scr. **23**, 1069 (1981).

[28] A. Ryabtsev, E. Kononov, R. Kildiyarova, W.-Ü. L. Tchang-Brillet, J.-F. Wyart, N. Champion, and C. Blaess, Atoms **3**, 273 (2015).

[29] W. Li, Z. Shi, Y. Yang, J. Xiao, T. Brage, R. Hutton, and Y. Zou, Phys. Rev. A **91**, 062501 (2015).

[30] M. L. Qiu, W. X. Li, Z. Z. Zhao, Y. Yang, J. Xiao, T. Brage, R. Hutton, and Y. Zou, J. Phys. B: At. Mol. Opt. Phys. **48**, 144029 (2015).

[31] M. Li, M. Qiu, J. Xiao, K. Yao, T. Brage, R. Hutton, and Y. Zou, Phys. Scr. **91**, 105401 (2016).

[32] Z. Z. Zhao, M. L. Qiu, R. F. Zhao, W. X. Li, X. L. Guo, J. Xiao, C. Y. Chen, Y. Zou, and R. Hutton, J. Phys. B: At. Mol. Opt. Phys. **48**, 115004 (2015).

[33] Q. Lu, J. He, H. Tian, M. Li, Y. Yang, K. Yao, C. Chen, J. Xiao, J. G. Li, B. Tu, and Y. Zou, Phys. Rev. A **99**, 042510 (2019).

[34] Q. Lu, C. L. Yan, J. Meng, G. Q. Xu, Y. Yang, C. Y. Chen, J. Xiao, J. G. Li, J. G. Wang, and Y. Zou, Phys. Rev. A **103**, 022808 (2021).

[35] Q. Lu, C. L. Yan, N. Fu, Y. Yang, C. Y. Chen, J. Xiao, K. Wang, and Y. Zou, J. Quant. Spectrosc. Radiat. Transfer **262**, 107533 (2021).

[36] X. Ding, F. Zhang, Y. Yang, L. Zhang, F. Koike, I. Murakami, D. Kato, H. A. Sakaue, N. Nakamura, and C. Dong, Phys. Rev. A **101**, 042509 (2020).

[37] Y. Kobayashi, K. Kubota, K. Omote, A. Komatsu, J. Sakoda, M. Minoshima, D. Kato, J. Li, H. A. Sakaue, I. Murakami, and N. Nakamura, Phys. Rev. A **92**, 022510 (2015).

[38] A. Komatsu, J. Sakoda, M. Minoshima, H. A. Sakaue, X.-B. Ding, D. Kato, I. Murakami, F. Koike, and N. Nakamura, Plasma Fusion Res. **7**, 1201158 (2012).

[39] M. Mita, H. A. Sakaue, D. Kato, I. Murakami, and N. Nakamura, Atoms **5**, 13 (2017).

[40] Priti, M. Mita, D. Kato, I. Murakami, H. A. Sakaue, and N. Nakamura, Phys. Rev. A **102**, 042818 (2020).

[41] K. Kozioł and J. Rzadkiewicz, At. Data Nucl. Data Tables **137**, 101372 (2021).

[42] A. E. Kramida and T. Shirai, At. Data Nucl. Data Tables **95**, 305 (2009).

[43] A. Kramida, Can. J. Phys. **89**, 551 (2011).

[44] A. E. Kramida and T. Shirai, J. Phys. Chem. Ref. Data **35**, 423 (2006).

[45] J. Sakoda, A. Komatsu, H. Kikuchi, and N. Nakamura, Phys. Scr. **T144**, 014011 (2011).

[46] D. Kilbane, J. D. Gillaspy, Yu. Ralchenko, J. Reader, and G. O'Sullivan, Phys. Scr. **T156**, 014012 (2013).

[47] D. Kilbane, G. O'Sullivan, J. D. Gillaspy, Yu. Ralchenko, and J. Reader, Phys. Rev. A **86**, 042503 (2012).

[48] J. Xiao, R. Zhao, X. Jin, B. Tu, Y. Yang, D. Lu, R. Hutton, and Y. Zou, in *Proceedings of the 4th International Particle Accelerator Conference, IPAC2013* (JACoW, Shanghai, China, 2013), pp. 434–436.

[49] P. Beiersdorfer, V. Decaux, S. R. Elliott, K. Widmann, and K. Wong, Rev. Sci. Instrum. **66**, 303 (1995).

[50] P. Beiersdorfer, V. Decaux, and K. Widmann, Nucl. Instrum. Methods B **98**, 566 (1995).

[51] D. H. Kwon, J. Quant. Spectrosc. Radiat. Transfer **208**, 64 (2018).

[52] B. M. Penetrante, J. N. Bardsley, D. DeWitt, M. Clark, and D. Schneider, Phys. Rev. A **43**, 4861 (1991).

[53] E. Shimizu, S. Ali, T. Tsuda, H. A. Sakaue, D. Kato, I. Murakami, H. Hara, T. Watanabe, and N. Nakamura, Astron. Astrophys. **601**, A111 (2017).

[54] A. Kramida, Yu. Ralchenko, and J. Reader, *NIST ASD Team, NIST Atomic Spectra Database (version 5.8)* (National Institute of Standards and Technology, Gaithersburg, MD, 2020), https://www.nist.gov/asd.

[55] S. P. Preval, N. R. Badnell, and M. G. O'Mullane, J. Phys. B:At. Mol. Opt. Phys. **52**, 025201 (2019).